Baroclinic Tide Generation at the Dolphin and Union Strait in the Southern Canadian Arctic Archipelago

Chengzhu Xu,[1,2] Yongsheng Wu,[3] William J. Williams,[4] Kurtis Anstey,[4] Di Wan[4] and David Greenberg[3]

ABSTRACT. We studied baroclinic tide generation at the Dolphin and Union Strait, a channel in the southern Canadian Arctic Archipelago that consists of a shallow sill. Utilizing both observational data and numerical simulations, we found that, due to the presence of strong stratification in the summertime, baroclinic tides are generated at both M2 and K1 frequencies as a result of the interaction between the amplified tidal currents and bottom topography. The M2 baroclinic current, which is comparable to the M2 barotropic current in terms of amplitude, is dominated by linear dynamics in the first baroclinic mode. The amplitude of the M2 baroclinic current increases as the strength of stratification increases. In contrast, the K1 baroclinic current has a smaller amplitude in general. Dynamics of the K1 baroclinic current are more complicated, possibly due to nonlinear effects as well as contributions from the higher baroclinic modes. On the other hand, increasing the strength of stratification leads to a noticeable reduction of K1 elevation in the nearby basin, but has a very minor effect on M2 elevation.

Keywords: Canadian Arctic Archipelago; Kitikmeot Sea; stratification; topography; baroclinic tides; energy flux; energy dissipation

RÉSUMÉ. Nous avons étudié la génération des marées baroclines dans le détroit de Dolphin et Union, un chenal du sud de l'archipel Arctique canadien consistant en un seuil peu profond. À l'aide de données d'observation et de simulations numériques, nous avons constaté qu'en raison de la présence d'une stratification forte pendant l'été, les marées baroclines sont générées aux fréquences M2 et K1 du fait de l'interaction entre les courants de marée amplifiés et de la topographie du fond. Le courant barocline M2, dont l'amplitude se compare au courant barotrope M2, est dominé par une dynamique linéaire dans le premier modèle barocline. L'amplitude du courant barocline M2 augmente à mesure que la force de la stratification augmente. Par contraste, le courant barocline K1 a une amplitude de moindre envergure en général. La dynamique du courant barocline K1 est plus compliquée, peut-être en raison des effets non linéaires et de l'apport des modèles baroclines plus élevés. Par ailleurs, l'augmentation de la force de la stratification mène à une réduction remarquable de l'élévation K1 dans le bassin avoisinant, mais un a effet très minime à l'élévation M2.

Mots-clés : archipel Arctique canadien; mer de Kitikmeot; stratification; topographie; marées baroclines; flux d'énergie; dissipation d'énergie

Traduit pour la revue *Arctic* par Nicole Giguère.

INTRODUCTION

The Canadian Arctic Archipelago (CAA) is a large continental shelf that consists of a number of islands and channels (Fig. 1a). These channels provide a key pathway for the movement of water masses from the Arctic Ocean to the northern Atlantic Ocean (McLaughlin et al., 2004). Due to the complexity of channel geometry and the roughness of bottom topography, tidal currents in the CAA experience local acceleration in many locations. For example, in the vicinity of Barrow Strait, tidal currents can reach 1.5 m s[1] (Prinsenberg and Bennett, 1989). Tides in the CAA originate from both the Atlantic Ocean and the Arctic Ocean, though the Atlantic tides have a major influence over the majority of the CAA (Guo et al., 2020).

Tidal propagation in the CAA is significantly affected by the extent of sea ice coverage. Based on acoustic Doppler current profiler (ADCP) data and numerical simulations, Rotermund et al. (2021) showed that, due to the roughness of sea ice, tidal elevation and currents could be damped by more than 50% in the winter.

Oceanographic conditions of the southern CAA are different from those of the northern CAA, primarily due to the seasonal variation of sea-ice coverage, which affects not only tidal propagation, but also near-surface stratification (Williams et al., 2018; Xu et al., 2021). During the ice-free season, strong stratification is formed near the sea surface due to freshwater input from ice melting, river runoff, and net precipitation, as well as surface warming because of to solar radiation. Stratification acts to reduce diapycnal

[1] College of Earth, Ocean, and Atmospheric Sciences, Oregon State University, 1500 SW Jefferson Way, Corvallis, Oregon, USA
[2] Corresponding author: chengzhu.xu@oregonstate.edu
[3] Fisheries and Oceans Canada, Bedford Institute of Oceanography, 1 Challenger Drive, Dartmouth, Nova Scotia, Canada
[4] Fisheries and Oceans Canada, Institute of Ocean Sciences, 9860 West Saanich Road, Sidney, British Columbia, Canada
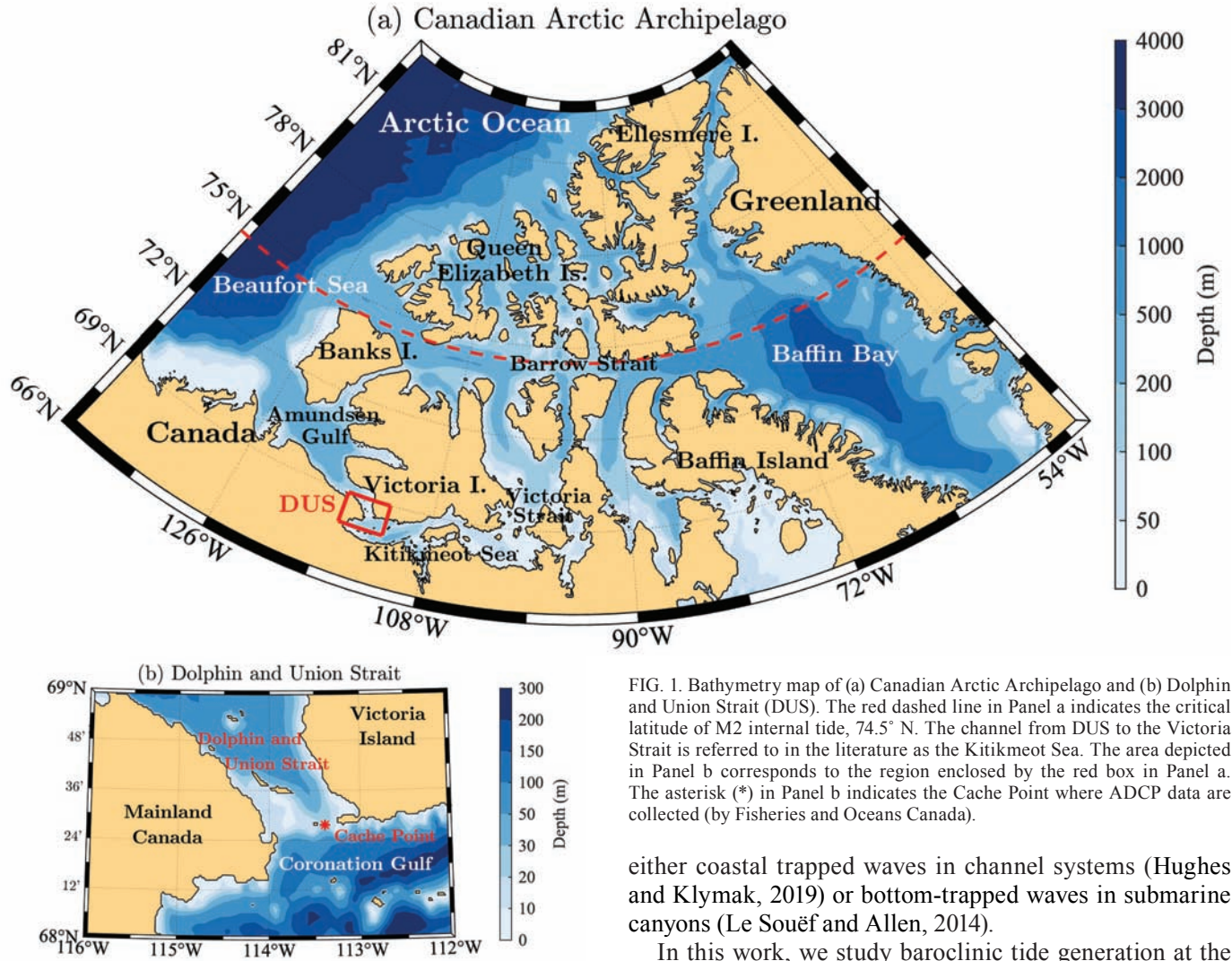
FIG. 1. Bathymetry map of (a) Canadian Arctic Archipelago and (b) Dolphin and Union Strait (DUS). The red dashed line in Panel a indicates the critical latitude of M2 internal tide, 74.5° N. The channel from DUS to the Victoria Strait is referred to in the literature as the Kitikmeot Sea. The area depicted in Panel b corresponds to the region enclosed by the red box in Panel a. The asterisk (*) in Panel b indicates the Cache Point where ADCP data are collected (by Fisheries and Oceans Canada).

mixing, thus limiting the nutrient flux and primary production (Bouchard et al., 2018; Back et al., 2021), except near narrow straits and shallow sills where tidal currents are strong (Hannah et al., 2009; Dalman et al., 2019).

On the other hand, the presence of stratification also provides potential for the generation of baroclinic (internal) tides where tide–topography interaction occurs. On the global scale, about a third of barotropic tidal energy is converted to baroclinic energy at rough topography (Egbert and Ray, 2000). Baroclinic tides may propagate away from the generation sites freely, provided that:

$$f \leq \omega \leq N \tag{1}$$

where ω is the tidal frequency, f is the Coriolis frequency, and N is the buoyancy frequency. In a stratified ocean, $\omega \ll N$ in general, but $\omega \leq f$ only within certain latitude bands. For example, the internal M2 tide can propagate freely between 74.5° S and 74.5° N, while the internal K1 tide can propagate freely between 30° S and 30° N only. Above the latitude where $\omega = f$ (i.e., the critical latitude), internal tides cannot propagate freely but may still exist in the form of

either coastal trapped waves in channel systems (Hughes and Klymak, 2019) or bottom-trapped waves in submarine canyons (Le Souëf and Allen, 2014).

In this work, we study baroclinic tide generation at the Dolphin and Union Strait (DUS) in the southern CAA. The strait is located between Victoria Island and mainland Canada, connecting the Kitikmeot Sea and the rest of the Arctic Ocean (Fig. 1b). In recent years, the Kitikmeot Sea has become a focal point of significant research efforts (e.g., Bouchard et al., 2018; Williams et al., 2018; Dalman et al., 2019; Back et al., 2021; Rotermund et al., 2021; Xu et al., 2021) due to its strategic location along the Northwest Passage and its vulnerability in a changing climate. At the south end of the DUS is a shallow sill, significantly limiting the exchange of fresh water, heat, and nutrients between the Kitikmeot Sea and the rest of the Arctic Ocean. Conversely, the sill amplifies tidal currents at the DUS, leading to enhanced vertical mixing, nutrient fluxes, and potentially elevated local biological productivity.

Utilizing both observational data and numerical simulations, we found that baroclinic tides are generated at both M2 and K1 frequencies at the DUS. The M2 baroclinic tide is dominated by linear dynamics in the first baroclinic mode. It propagates freely and carries most of the baroclinic energy away from the generation site. In contrast, the K1 baroclinic tide cannot propagate freely, since the DUS is located beyond the critical latitude for the K1 baroclinic

tide. As a result, a significant amount of baroclinic energy is dissipated locally near the generation site, leading to a decrease in tidal elevation in the nearby basin.

Channel Geometry

The Dolphin and Unions Strait (DUS) is located at 69° N, which is below the critical latitude for M2 internal tide (74.5° N; indicated by the dashed line in Fig. 1a) but beyond the critical latitude for K1 internal tide (30° N). At this latitude, the Coriolis frequency is 1.357×10^{-4} s^{-1}. The channel is over 100 km long and about 40 km wide. Near the Coronation Gulf is a shallow sill about 20 m deep, while the average depth of the nearby basin at the Coronation Gulf is about 200 m. The topography to the south of the sill (connecting the Coronation Gulf) is relatively smooth and has an average slope of 0.005, whereas topography on the north side is more complex. Tidal currents at the DUS are dominated by M2 and K1 constituents, both of which have a maximum amplitude of approximately 0.5 m s^{-1} (Rotermund et al., 2021). On top of the sill, the water column is generally unstratified due to mixing caused by the strong tidal currents, whereas in the nearby basins, near-surface stratification tends to be strong in the summer.

Internal Wave Parameters

Internal wave generation is usually characterized by several dimensionless parameters. Here, we discuss two of them. The steepness parameter, ϵ_1, is defined by:

$$\epsilon_1 = \frac{\gamma}{\alpha} \qquad (2)$$

where γ is the topographic slope and α is the internal wave characteristic slope, given by:

$$\alpha = \sqrt{\frac{\omega^2 - f^2}{N^2 - \omega^2}} \qquad (3)$$

In this equation, the buoyancy frequency N is defined by:

$$N(z) = \sqrt{-\frac{g}{\rho_0}\frac{d\bar{\rho}}{dz}} \qquad (4)$$

where g is the acceleration due to gravity, ρ_0 is the reference density and $\bar{\rho}(z)$ is the undisturbed background density profile, whose horizontal variation is neglected. In a non-uniform stratification, N is typically evaluated at the crest of the topography (Pétrélis et al., 2006). Using the summer stratification in the nearby basins as the background stratification, typical values of N at 20 m of depth are on the order of 0.1 s^{-1}. Hence, for M2 internal tide, which has a frequency 1.405×10^{-4} s^{-1}, the internal wave characteristic slope at the DUS is 3.65×10^{-4}. For topography with a slope of 0.005, this implies that $\epsilon_1 < 1$ and the topography is subcritical.

The tidal excursion parameter, ϵ_2, is defined by:

$$\epsilon_2 = \frac{U_0 k_b}{\omega} \qquad (5)$$

where U_0 is the maximum magnitude of local barotropic flow, and k_b^{-1} is the horizontal scale of topography, which can be estimated by $k_b = \gamma/h_0$, where h_0 is the topographic amplitude. On the south side of the sill at the DUS, the horizontal scale of the topography is on the order of 10 km. Given that $U_0 \approx 0.5$ m^{-1} at the DUS, for M2 internal tide $\epsilon_2 < 1$ as well. Together, these two non-dimensional parameters suggest that nonlinear effects are insignificant and the M2 internal tide is generated mainly at the forcing frequency (Vlasenko et al., 2005; Garrett and Kunze, 2007). By comparing theoretical description with simulation results, we will show that M2 baroclinic tide generated on the south end of the DUS can indeed be described by linear theory. Conversely, dynamics of the K1 internal tide are more complicated since the DUS is above the critical latitude and the K1 internal tide is sub-inertial.

Internal Wave Structures

For freely propagating internal waves in which nonlinear effects are insignificant, wave dynamics can be described by omitting the nonlinear advection terms in the governing equation. The linearized equations of motion admit plane wave solutions of the form:

$$\cos(kx + ly - \omega t) \qquad (6)$$

for describing the horizontal structures, where k and l are horizontal wave numbers in the x and y directions, respectively. The vertical structure of internal waves can be described by solutions of the eigenvalue problem often referred to as the Taylor–Goldstein equation (e.g., Cushman-Roisin and Beckers, 2011; Kundu et al., 2012). In a zero or constant background current, the Taylor–Goldstein equation is given by:

$$\frac{d^2\phi}{dz^2} + (k^2 + l^2)\alpha^{-2}\phi = 0 \qquad (7)$$

and the boundary conditions at the surface and the bottom boundary are given by:

$$\phi(0) = \phi(-H) = 0 \qquad (8)$$

In this equation, the eigenfunction $\phi(z)$ characterizes the vertical structure of the wave-induced velocity field, such that the amplitude of the horizontal velocity is proportional to its first-order derivative, $d\phi/dz$. Given physically relevant N and ω, Equation 7 has an infinite set of discrete eigenvalues, each of which corresponds to a distinct baroclinic mode number. The mode number can be loosely interpreted as the number of shear layers inside the water column, across which
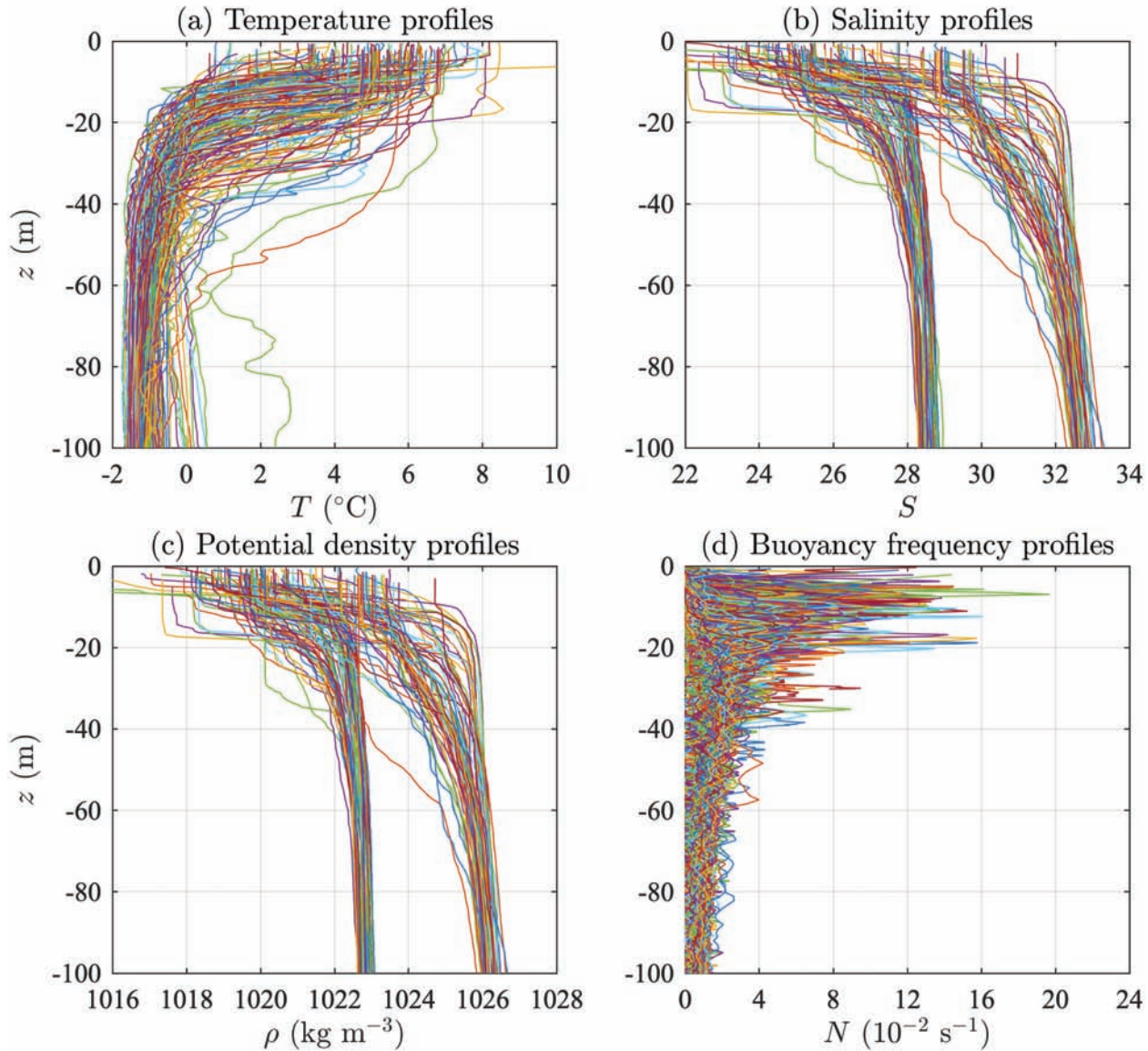
FIG. 2. Vertical profiles of (a) temperature, (b) salinity, (c) potential density, and (d) buoyancy frequency, measured at various locations in the Amundsen Gulf and the Coronation Gulf.

the horizontal velocity changes sign. Mode-1 internal waves consist of a single shear layer, usually located at, or near, the pycnocline. For nonlinear stratification, α is a function of depth, such that the Taylor–Goldstein equation is nonlinear and does not have analytical solutions. In the present work, it is solved numerically using a pseudo-spectral technique (Trefethen, 2000).

METHODS

Observed Stratification

We consider stratification of the nearby basins in the Coronation Gulf and Amundsen Gulf as the background stratification for our study. The Institute of Ocean Sciences and partner organizations have been collecting conductivity, temperature, and depth (CTD) data in these regions since 1965. The data are available and accessible through the Canadian Integrated Ocean Observing System (CIOOS Pacific, 2024). We examined 150 vertical profiles at various locations between $108°–122°$ W and $67.5°–71°$ N, focussing on the summer stratification only. We excluded data collected from October to June due to their relatively small sample sizes. We calculated the potential density following the TEOS-10 standard using the Gibbs Seawater Oceanographic Toolbox (McDougall and Barker, 2011). We computed buoyancy frequency using a central difference method based on Equation (4).

The CTD data suggest that typical density profiles in the summer are characterized by strong near-surface stratification (Fig. 2). In the upper layer, temperature, salinity, and density all vary significantly, and their specific values depend on the location and time that the data are
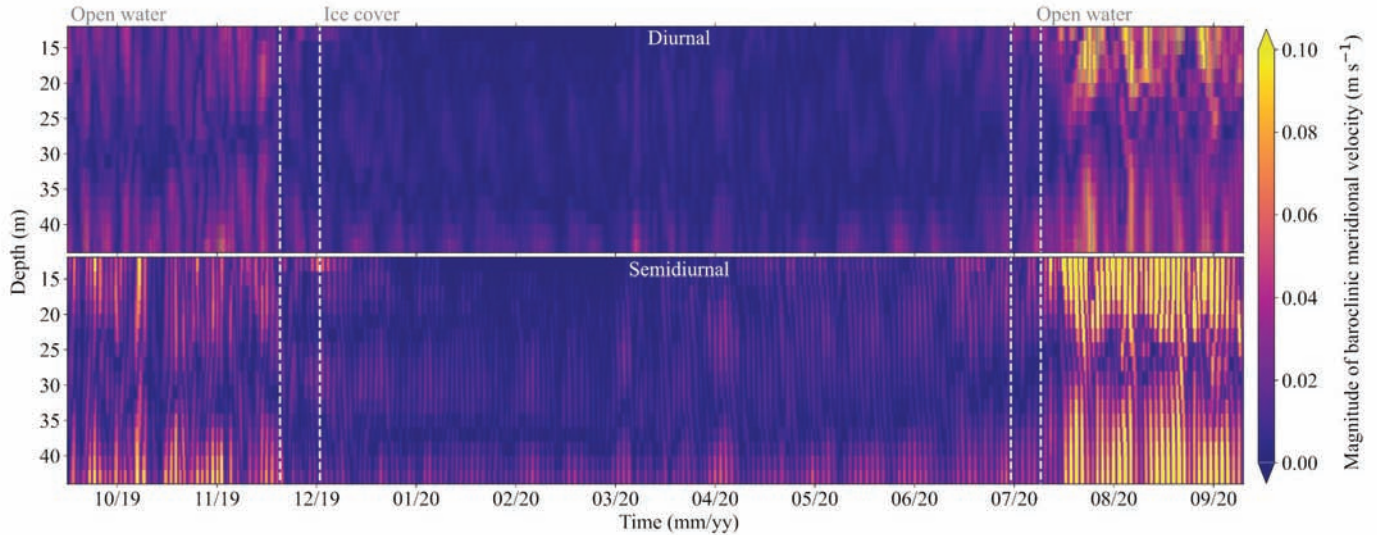
FIG. 3. Observed vertical profiles of K1 and M2 barotropic and baroclinic meridional amplitude and phase at the Cache Point ADCP mooring in 2019–20.

collected. The lower layer exhibits less variation in general, although two different water masses can be identified from the salinity and density profiles. At the depth of 100 m, density is about 1023 kg m^{-3} for one of them and 1026 kg m^{-3} for the other. The former is from the Coronation Gulf while the latter is from the Amundsen Gulf. The exchange between the two water masses is limited because of the presence of the sill at the DUS. The buoyancy frequency profiles (Fig. 2d) suggest that the pycnocline is typically located within the upper 20 m, where the buoyancy frequency is on the order of 0.1 s^{-1}. The lower layer is weakly stratified in general, with buoyancy frequency that is one order of magnitude smaller. On average, the density difference between the upper and lower layers is about 4 kg m^{-3}, or 4% of the background density, with a standard deviation of 1.7 kg m^{-3}.

Observed Tidal Currents

We obtained observed velocity data from a Fisheries and Oceans Canada mooring on the south slope of the sill in 41 m of water, at 113.39° W, 68.47° N (the Cache Point indicated in Fig. 1b), deployed from September 2019 to September 2020. An upward looking 600 kHz ADCP sat at a depth of 38 m, with 2 m vertical resolution and 15 min ensembles of 7.5 sec pings. We processed data for QA/QC, including adjustments for northern magnetic effects and masking for surface side-lobe and ice-related intensity spikes. We determined barotropic velocity from the depth average through the water column, and baroclinic velocity from the difference between the total and depth-averaged velocities. We obtained diurnal and semi-diurnal velocities using an 8th order Butterworth digital band-pass filter with cut-off frequencies (determined from power spectra of observations) of [9.00$e-$6, 1.50$e-$5] and [1.95$e-$5, 2.60$e-$5] Hz, or [0.78, 1.30] and [1.68, 2.25] cpd, for diurnal and semidiurnal, respectively.

The time series of baroclinic velocities (Fig. 3) shows a strong seasonal signal in both M2 and K1 constituents. In general, the baroclinic currents are strong from August to November, when there is no ice coverage and the near-surface stratification is strong, and weak from December to July, when the sea surface is covered by ice and stratification is weak. Similar conclusions can be drawn from the vertical profiles of the baroclinic velocities shown in Figure 4. We determined summer tidal profiles of K1 and M2 amplitude and phase (Fig. 4a) from tidal decompositions during open water periods (September to November 2019 and July to September 2020), while we determined winter profiles (Fig. 3b) from the ice-covered period (December 2019 to June 2020).

During the ice-free season, the upper and lower layers of both M2 and K1 baroclinic velocities are clearly identifiable by their opposite phases. The phase shift occurs between 25–30 m, where the amplitude is minimal, indicating the existence of a shear layer at this depth. These are the typical characteristics of mode-1 internal waves. In contrast, during the ice-covered season, the baroclinic velocity has much smaller amplitudes across the entire water column. Two local minima can be seen from the amplitude profiles, while phase shift can also be found at two different depths corresponding to the minimum amplitudes, implying that the baroclinic currents are much weaker and that they are likely to be dominated by mode-2 waves. In numerical simulations discussed later, we will focus on the ice-free season only, when near-surface stratification and the baroclinic currents are strong.

Numerical Model Setup

The numerical model adopted in this study is developed based on the Finite Volume Community Ocean Model (FVCOM; Chen et al., 2003, 2007). The model domain covered the entire Kitikmeot Sea (Fig. 5). The model
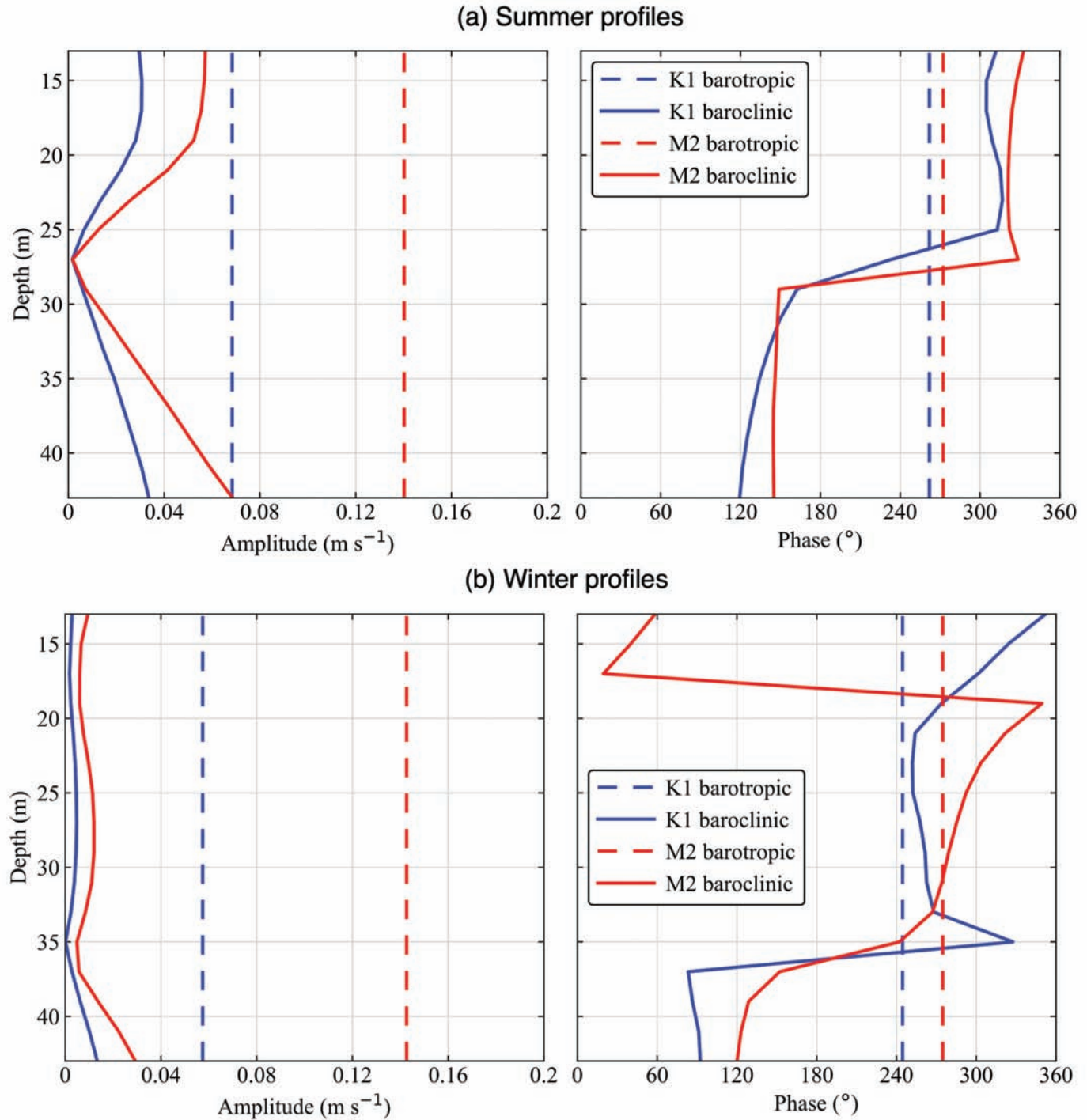
(a) Summer profiles

(b) Winter profiles

FIG. 4. Observed magnitude of diurnal and semidiurnal baroclinic meridional velocities at the Cache Point ADCP mooring (indicated by the asterisk in Figure 1b) in 2019–20.

bathymetry was obtained from the Canadian Hydrographic Service (CHS). For the part of the model domain where data from CHS were not available, bathymetry data from TPXO9 (Egbert et al., 1994; Egbert and Erofeeva, 2002) were adopted. Unstructured grid is adopted in the horizontal directions. The length of each element varied from hundreds of meters in near-shore waters to several kilometers in open waters, depending on the variation of channel width, the complexity of coastline, the water

depth, and the bottom steepness. In the vertical direction, generalized sigma coordinates with 40 layers were employed (Fig. 6). By clustering several equally spaced levels (i.e., z-levels) near the surface, the generalized sigma coordinates can reduce horizontal pressure gradient errors that commonly occur in regular sigma coordinates (Haney, 1991; Beckmann and Haidvogel, 1993; Song, 1998; Mellor et al., 2002; Ezer and Mellor, 2004). In the model, tides were forced at lateral open boundaries by harmonic
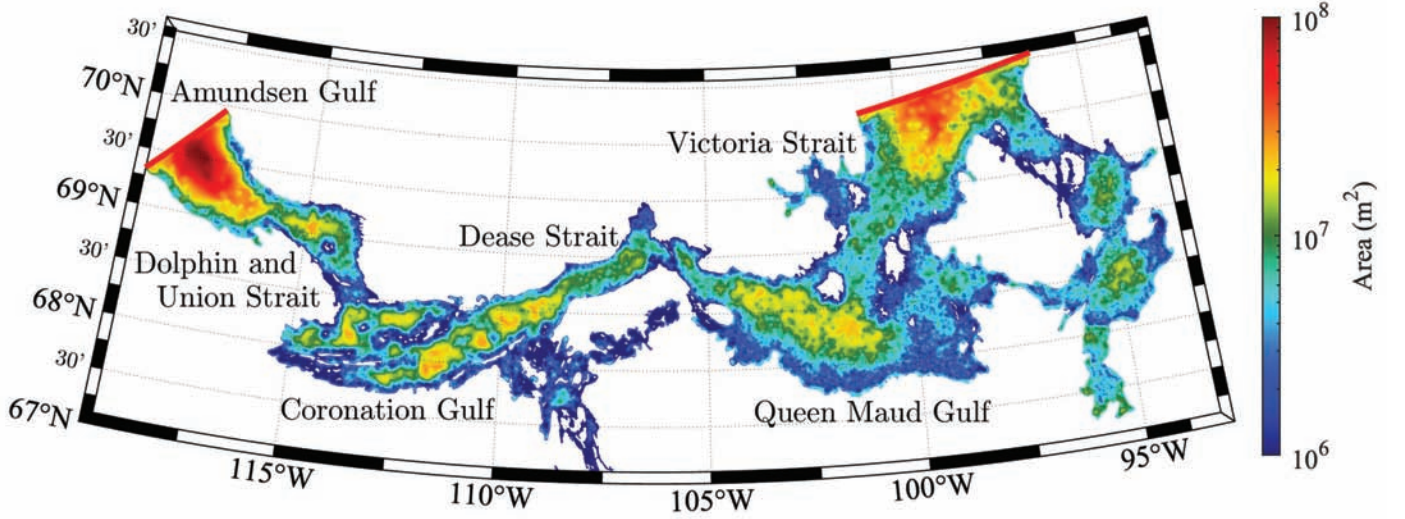
FIG. 5. Model domain and resolution. Locations of the lateral open boundaries are indicated by the red line segments. The pseudocolor represents the area of node-based control volume. Except near the open boundaries, the area is on the order of 10^6 m² (blue) to 10^7 m² (green), which means that the side lengths of the elements are on the order of 1 km.
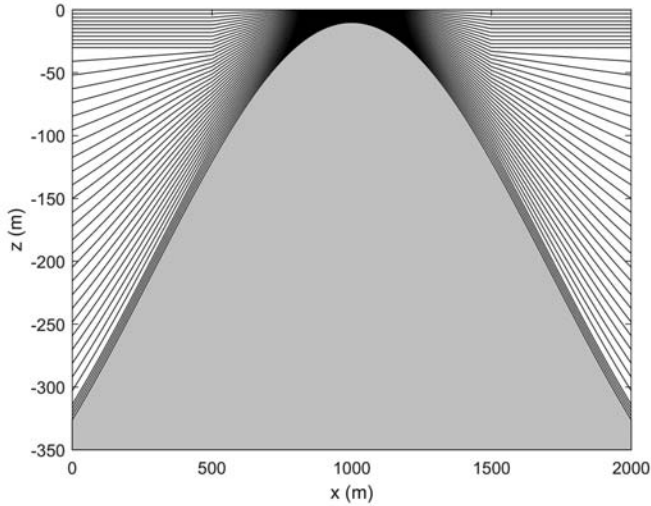

FIG. 6. Schematic of generalized sigma coordinates. In deep waters, equally spaced levels are placed along the surface and the bottom boundaries, in order to reduce horizontal pressure gradient errors and to better represent the bottom friction. In shallow waters, the regular sigma coordinates are adopted.

constants (amplitudes and phases) of eight major tidal constituents (M2, S2, N2, K2, O1, K1, P1, and Q1) derived from TPXO9. The surface forcing was turned off in order for the model to simulate ocean circulations forced purely by barotropic tides, and the bottom friction was represented by the logarithmic layer formula, with the darg coefficient given by:

$$C_D = \left[\frac{\kappa}{\ln(0.5 z_b / z_0)} \right]^2 \qquad (9)$$

where $\kappa = 0.4$ is the von-Karman constant, z_b is the thickness of the bottom layer, and z_0 is the length scale of the bottom roughness. Ideally, z_0 should be a function of grain sizes of the bottom sediment, types of the bed form,

and intensity of the bottom velocity (Pringle et al., 2018). Due to the lack of sediment data, however, z_0 was assumed to be spatially uniform in this study. The value 8.5×10^{-3} m was adopted based on trial and error by comparing the modeled and observed water elevations. The Smagorinsky diffusivity was used to estimate the horizontal diffusion. An embedded second-order turbulence closure scheme was applied in the vertical direction. To simulate the flooding and drying processes in the tidal flats, a mass-conserving wetting and drying treatment was employed.

We initialized the model from several different density profiles, including a case of constant density profile (barotropic case) and three cases of variable density profiles (baroclinic cases). For all cases, stratification was horizontally uniform. For the baroclinic cases, we focused on mode-1 baroclinic tide generation due to near-surface stratificaiton. To simplify the problem, we neglected stratification of the lower layer and set the lower layer density to $\rho_1 = 1025$ kg m⁻³ for all cases. The initial density profiles in the baroclinic cases followed the hyperbolic tangent function of the form:

$$\rho(z) = \rho_1 - \frac{1}{2} \Delta\rho \left[\tanh\left(\frac{z - z_p}{0.5d} \right) + 1 \right] \qquad (10)$$

where $\Delta\rho$ is the density difference between the upper and lower layers, $z_p = -15$ m is the location of the pycnocline center, and $d = 4$ m is the thickness of the pycnocline. We adopted three different values of $\Delta\rho$ in order to create stratification of different strengths (Table 1). In practice, because the density field cannot be specified directly in the model, we determined the initial density field by prescribing the corresponding temperature and salinity fields based on trail and error (see Table 1). The near-surface stratification determined by Equation 10 represents the aforementioned observation on stratificaition, even though the exact density

TABLE 1. Parameters of the three baroclinic cases, where ΔT, ΔS, and $\Delta \rho$ denote differences of temperature, salinity, and density, respectively, between the upper and lower layers, and N_0 is the buoyancy frequency measured at the pycnocline center, $z_p = -15$ m. Cases are labeled based on the strength of stratification. For all cases, temperature and salinity of the lower layer are set to $T_1 = 0°C$ and $S_1 = 31.3$, respectively, which yields the density of $\rho_1 = 1025$ kg m^{-3}.

Case name	ΔT (°C)	ΔS	$\Delta \rho$ (kg m^{-3})	N_0 (10^{-2} s^{-1})
Low-N	0	2	1.6	6.0
Mid-N	−6	4.5	4.0	9.4
High-N	−13	11	10.0	14.9

profiles were different. In particular, the pycnocline were located at approximately the crest of the bottom topography, and the buoyancy frequency N measured at the pycnocline center had the same order of magnitude as the observation. Because the surface forcing is turned off, diapycnal mixing

will decrease the density gradient across the pycnocline over time. For this reason, we performed our simulations for 45 days, long enough for harmonic analysis to be sufficiently accurate, but short enough for stratification to retain its strength.

RESULTS

Simulation Results

For the case labeled as *Mid-N* in Table 1, the density difference between the surface and bottom layers is 4 kg m^{-3}, which is equal to the average density differences we calculated through observation (based on data from the Canadian Integrated Ocean Observing System, as discussed earlier). Snapshots of the velocity fields from this case at two different times, shown in Figure 7, suggest that the tidal currents on top of the sill are extremely strong,
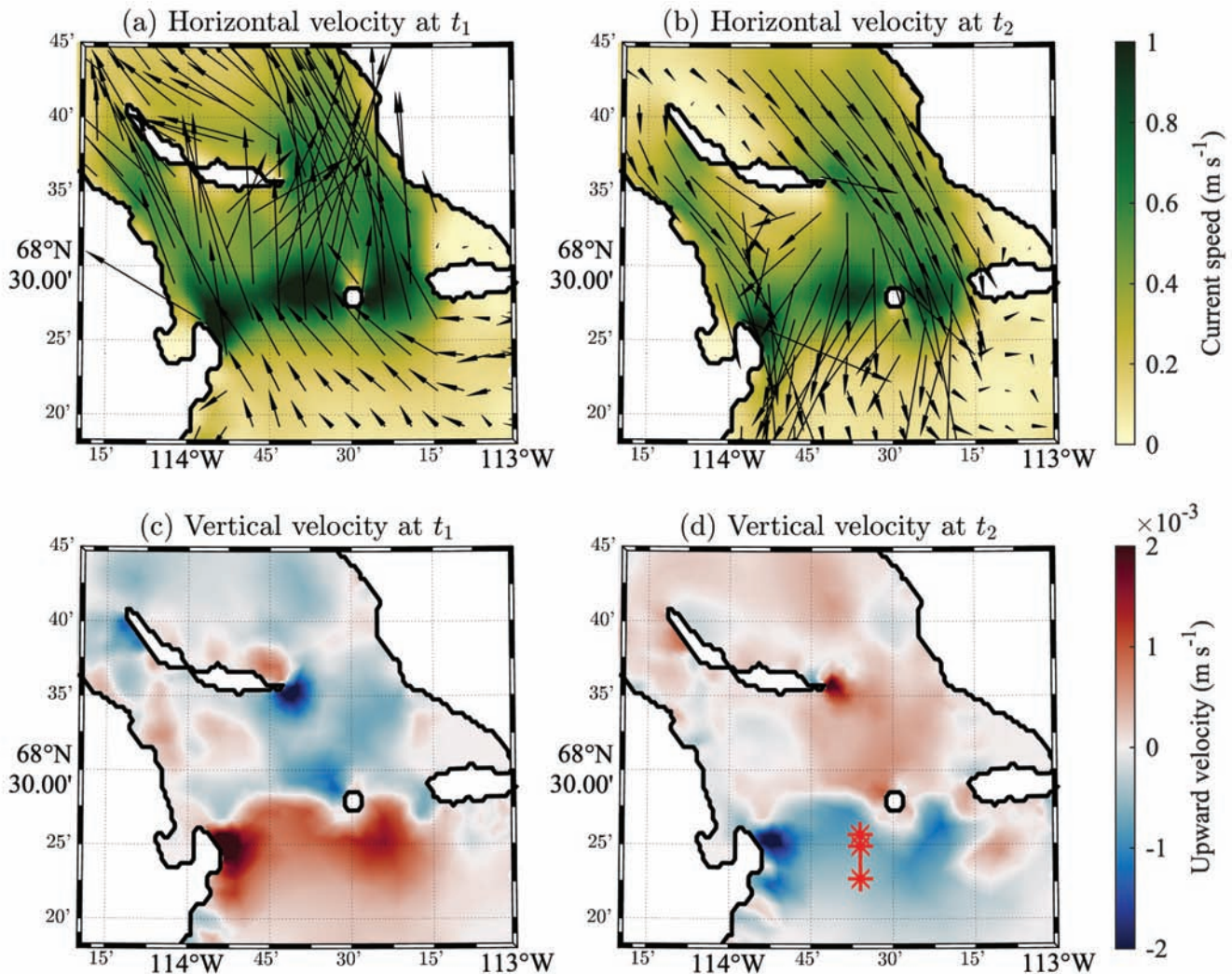

FIG. 7. Depth average of (a)−(b) horizontal and (c)−(d) vertical velocities at two different times, $t_1 = 121$ hr and $t_2 = 139$ hr after the simulations started, for the case labeled as *Mid-N* in Table 1. The asterisks (*) along the transect in Panel d indicate the locations of P1, P2, and P3, where we analyze vertical structures of the internal tides.
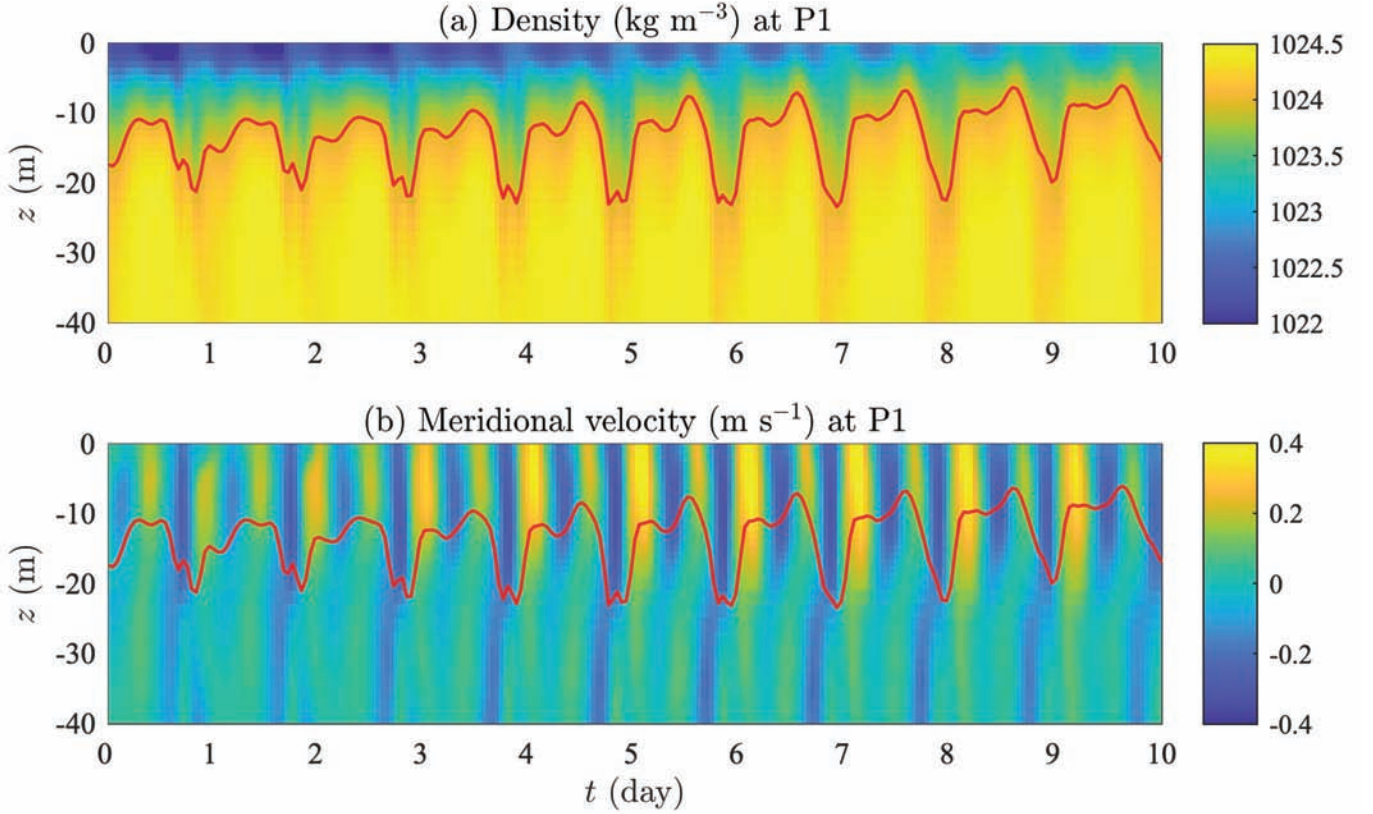
FIG. 8. Hovmöller diagrams of (a) density and (b) meridional velocity profiles at P3 (marked by the asterisk in Fig. 7) for the first 10 days of the *Mid-N* case. In Panel b, northward velocity is shown in yellow and southward is shown in blue. The red curves indicate the isopycnal of density 1024 kg m^{-3}. For clarity of presentation, only the upper 40 m of the water column is shown.

with the maximum velocity reaching 1 m s^{-1}. Tidal currents can cause upwelling and downwelling occurring on both sides of the sill. The interaction between tidal currents and bottom topography thus provides significant potential for baroclinic tide generation.

To analyze the vertical structures of internal tides, we focus on three points along the transect indicated in Figure 7(d). From north to south, we denote these locations as P1 (113.59° W, 68.43° N), P2 (113.59° W, 68.41° N), and P3 (113.59° W, 68.38° N), where total water depths are 23 m, 37 m, and 74 m, respectively. The length of the transect is approximately 10 km, and the topographic slope along the transect is about 0.005. The timeseries in Figure 8 shows that at P3, vertical profiles of both density and current are depth-dependent, and that they fluctuate on a semi-diurnal to diurnal time scale. Measured based on the isopycnal of density 1024 kg m^{-3} (red curves), the interface displacement occurs with the tidal cycles and is roughly ±5 m about its resting depth of approximately 15 m. Figure 8b shows the presence of an amplitude difference and phase lag of the current velocity across the density interface, implying that baroclinic flows exist consistently over time.

Through spectral analysis of the meridional velocity at P3, we found that baroclinicity of tidal currents exists in all simulations except for the barotropic case. We computed the power spectral density of meridional velocity using the fast Fourier transform algorithm, and Figure 9 shows

results of tidal periods between 10 and 36 hours. Although barotropic M2 and K1 currents have similar strength, as suggested by the barotropic case, they behave differently in the baroclinic cases, where the M2 current in the upper layer is much stronger than that in the lower layer or the K1 current throughout the entire water column. Moreover, the strength of baroclinicity, indicated by the difference of power spectral density between the upper and lower layers, increases with the strength of stratification from the *Low-N* case to the *High-N* case. On the other hand, the K1 signal remains largely barotropic, and the dependence of baroclinicity on the stratification is not clear.

Vertical Structures

To analyze the vertical structures of the baroclinic currents, we decompose the total velocity into a barotropic component and a baroclinic component. Following standard convention in the literature, we define the former as the depth average of the total velocity, and the latter as the difference between them, though we note that in shallow waters, due to the relative thickness of the bottom boundary layer, the bottom friction may have significant influences on both barotropic and baroclinic velocities. We then performed harmonic analysis of both barotropic and baroclinic velocities using the t-tide package (Pawlowicz et al., 2002). Given the orientation of the channel, we
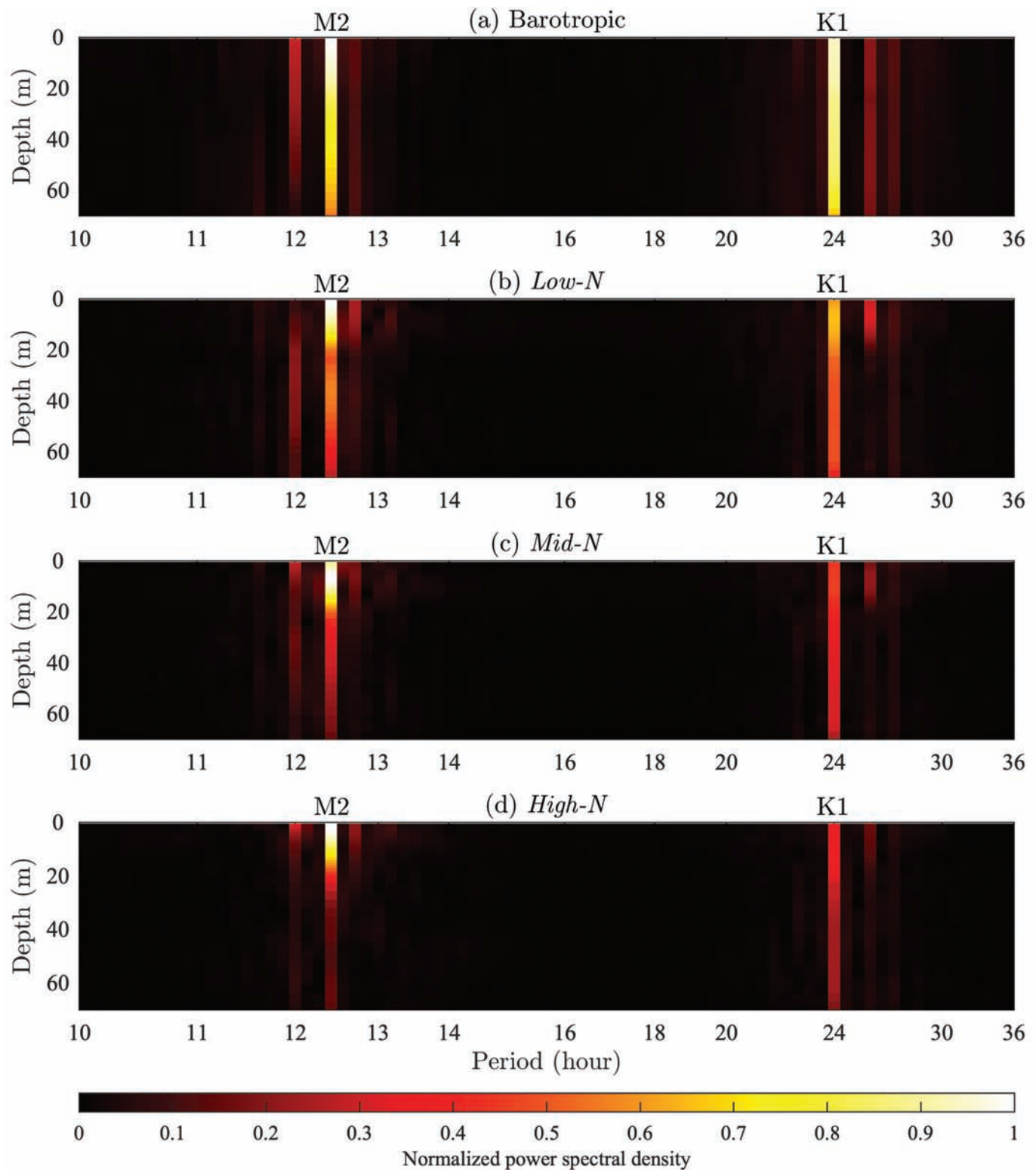
FIG. 9. Power spectral density of the meridional velocity at P3, computed from the first 45 days of all simulations. In each panel, the power spectral density is normalized by its maximum value.

performed analyses of the meridional velocity only.

Figure 10 shows that, except for the K1 amplitude at P3 (Panel f), vertical structures of the baroclinic velocities have characteristics that are typical of a mode-1 internal wave, similar to those from the observation shown in

Figure 4a. That is, the amplitude has a local minimum near the pycnocline, where a shear layer exists, separating the opposite propagating currents across it. For the M2 tides, the amplitude of baroclinic velocities increases as the strength of stratification increases at all locations, with the
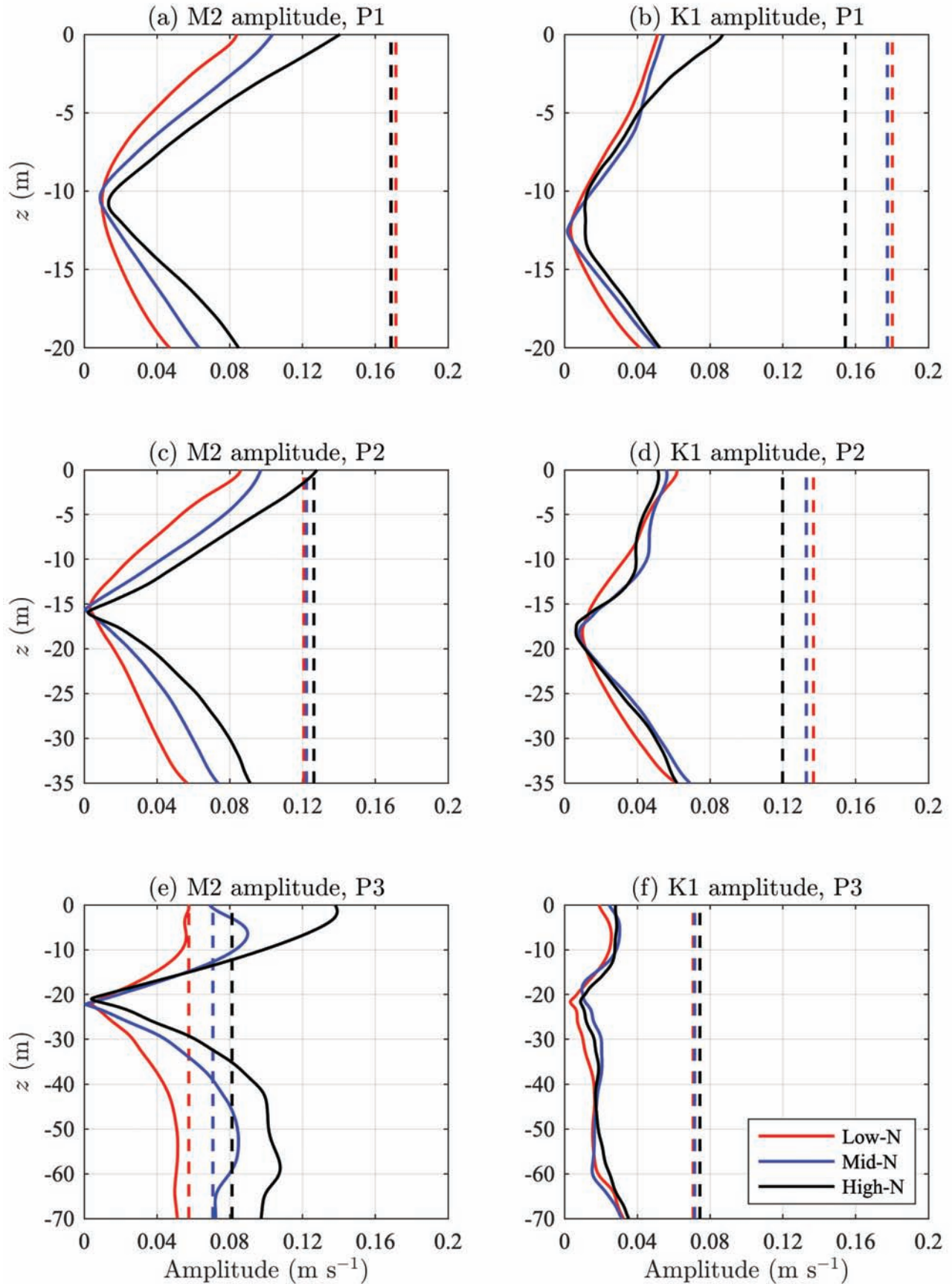
FIG. 10. Amplitudes of the M2 and K1 barotropic (dashed) and baroclinic (solid) velocities at P1, P2, and P3, from simulation results of the baroclinic cases.

maximum amplitude near the surface exceeding 0.1 m s^{-1} in the *High-N* case. The K1 amplitude of baroclinic velocities is generally smaller and exhibits weaker dependence on the stratification. At P3, which is about 10 km away from the topography crest, the K1 baroclinic velocities no longer have a clearly identifiable mode-1 structure, regardless of the strength of stratification. This is an indication that the K1 baroclinic tide cannot maintain its structure as it propagates away from the generation site and is likely to degenerate locally.

In fact, it can be shown that for the M2 baroclinic current, the simulated vertical structures at P3 match the theoretical prediction almost exactly. To reconstruct M2 baroclinic velocity, v_{M2}, from simulation results, we multiplied the M2 amplitude by the cosine of M2 phase θ, i.e.,

$$v_{M2} = A\cos\theta \qquad (11)$$

At any given time, strength of the M2 baroclinic current is proportional to the vertical profiles of v_{M2}, which are shown by the solid curves in Figure 11b. We obtained the corresponding structure function ϕ shown in Figure 11a by integrating v_{M2} over the entire water column. We obtained a theoretical prediction of the vertical structure function and velocity amplitude (dashed curves in Fig. 11) by solving the Taylor–Goldstein equation using background density profiles given by Equation (10) and parameters shown in Table 1, except that we increased pycnocline thickness to $d = 32$ m to account for the diapycnal mixing that occurred in the simulation. Although a time varying background current existed in the simulations, it was dominated by the barotropic velocities, except near the bottom boundary where the effect of bottom friction becomes important.

Hence, Taylor–Goldstein equation in the form of Equation (7) is applicable to the analysis, at least in the middle of the water column where the stratification is strong, and the effects of the bottom friction and a free surface are not significant.

Solutions of the Taylor–Goldstein equation shown in Figure 11 are for mode-1 only, while higher modes are omitted. Nevertheless, both the structure function and velocity amplitudes match those reconstructed from the simulation results almost exactly, at least for the *Mid-N* and *High-N* cases in the middle of the water column. Thus the simulation results imply that the overall dynamics of M2 baroclinic tide are dominated by mode-1, linear wave dynamics, provided that the stratification is reasonably strong. These results are consistent with the internal wave generation characterized by the steepness parameter $\in_1$ and the tidal excursion parameter $\in_2$ discussed in the introduction. For the *Low-N* case in which the stratification is relatively weak, higher mode waves might be non-negligible and could be the reason of the mismatch between the theory and the model results. For the K1 baroclinic tide, which is sub-inertial, Equation 7 is not applicable since it only describes the dynamics of freely propagating internal waves.

Water Elevation

Another effect of stratification is the decrease of K1 elevation in the Coronation Gulf, likely a consequence of the reduced tidal energy flux and increased local dissipation due to the generation of K1 internal tide. In the barotropic case, K1 elevation in the Coronation Gulf is roughly 20 cm. In the baroclinic cases, K1 elevation decreases
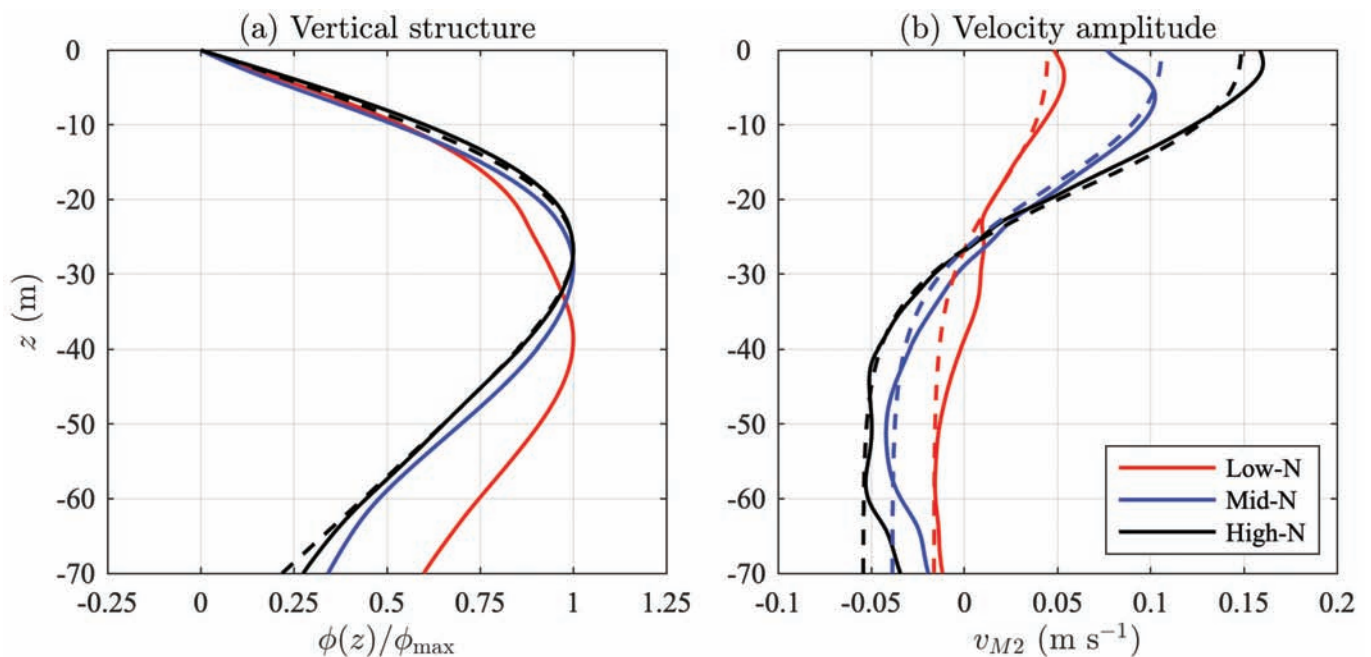

FIG. 11. Comparison of (a) structure function and (b) velocity amplitude of the M2 baroclinic current at P3 between simulation results (solid) and solutions of the Taylor-Goldstein equation (dashed). In Panel a, dashed curves overlap each other and only the black curve is visible.
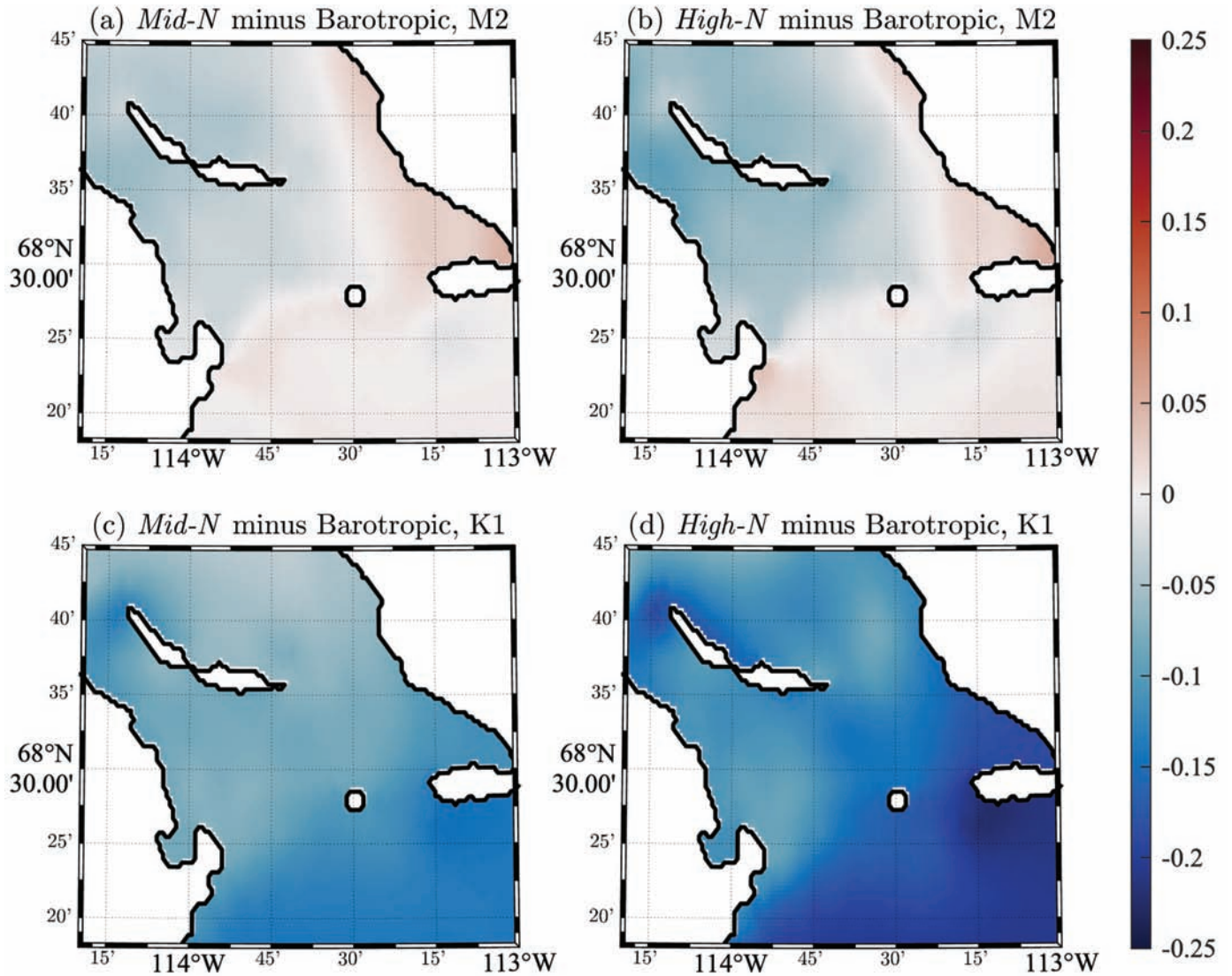
FIG. 12. Difference of tidal elevation between the baroclinic cases and the barotropic case for (a)–(b) M2 tide and (c)–(d) K1 tide, normalized by the local tidal elevation in the barotropic case.

consistently as the strength of stratification increases (Fig. 12). On average, in the *Low-N*, *Mid-N*, and *High-N* cases, K1 elevation is 8%, 12%, and 18% less than that in the barotropic case, respectively. In contrast, change of M2 elevation due to the stratification effect is much smaller. On average, differences of M2 elevation between baroclinic and barotropic cases are about 1% only, regardless of the strength of stratification.

CONCLUSIONS

By examining observation data and performing numerical simulations, we investigated baroclinic tide generation at the DUS due to tide–topography interaction and the presence of strong near-surface stratification in the summertime. Analysis of the observation data suggested that for both M2 and K1 tides, baroclinic currents are strong in the summer but weak in the winter, likely because summer stratification is much stronger than winter stratification. Based on the observed summer stratification, we designed a suite of numerical simulations utilizing an FVCOM-based numerical model. The simulation results suggested that near the generation site, M2 and K1 baroclinic currents both have clearly identifiable mode-1 structures. For M2 tide, the amplitude of the baroclinic velocity increases as the strength of stratification increases. Conversely, the K1 baroclinic current is weaker in general, and cannot maintain a consistent vertical structure away from the generation site. Analysis of water elevation suggests that increasing the strength of stratification leads to noticeable reduction of K1 elevation in the Coronation Golf, whereas M2 elevation remains almost unchanged.

Given the importance of the DUS in connecting the Kitikmeot Sea to the rest of the Arctic Ocean, our findings provide some insights into the physical oceanographic conditions of this area. Futrue research on this topic could focus on the greater CAA, since different channel geometry

and bottom topography could change results. Moreover, the effects of stratification and the Earth's rotation might also be different, especially in the northern CAA, which is covered by multi-year ice (Howell et al., 2013) and is located above the critical latitude of the M2 baroclinic tide. Additionally, for sub-inertial tides (K1 in the entire CAA and M2 in the northern CAA), we have not been able to quantify the relative importance of local dissipation versus baroclinic energy flux in the form of coastal trapped waves. Further research on this topic is needed, which may employ analyses of the complete energy budget (e.g., Kang and Fringer, 2012).

ACKNOWLEDGEMENTS

REFERENCES

Back, D.-Y., Ha, S.-Y., Else, B., Hanson, M., Jones, S.F., Shin, K.-H., Tatarek, A., et al. 2021. On the impact of wastewater effluent on phytoplankton in the Arctic coastal zone: A case study in the Kitikmeot Sea of the Canadian Arctic. Science of the Total Environment 764: 143861.
https://doi.org/10.1016/j.scitotenv.2020.143861

Beckmann, A., and Haidvogel, D.B. 1993. Numerical simulation of flow around a tall isolated seamount. Part I: Problem formulation and model accuracy. Journal of Physical Oceanography 23(8):1736–1753.
https://doi.org/10.1175/1520-0485(1993)023%3C1736:NSOFAA%3E2.0.CO;2

Bouchard, C., Geoffroy, M., LeBlanc, M., and Fortier, L. 2018. Larval and adult fish assemblages along the Northwest Passage: The shallow Kitikmeot and the ice-covered Parry Channel as potential barriers to dispersal. Arctic Science 4(4):781–793.
https://doi.org/10.1139/as-2018-0003

Chen, C., Huang, H., Beardsley, R.C., Liu, H., Xu, Q., and Cowles, G. 2007. A finite volume numerical approach for coastal ocean circulation studies: Comparisons with finite difference models. Journal of Geophysical Research 112: C03018.
https://doi.org/10.1029/2006JC003485

Chen, C., Liu, H., and Beardsley, R.C. 2003. An unstructured grid, finite-volume, three-dimensional, primitive equations ocean model: Application to coastal ocean and estuaries. Journal of Atmospheric and Oceanic Technology 20(1):159–186.
https://doi.org/10.1175/1520-0426(2003)020%3C0159:AUGFVT%3E2.0.CO;2

Cushman-Roisin, B., and Beckers, J.-M. 2011. Introduction to geophysical fluid dynamics, 2nd ed. New York: Academic Press.

CIOOS Pacific. 2024. Regional association of the Canadian integrated ocean observing system.
https://data.cioospacific.ca/erddap/files/IOS_CTD_Profiles/

Dalman, L.A., Else, B., Barber, D., Carmack, E., Williams, W., Campbell, K., Duke, P.J., Kirillov, S., and Mundy, C.J. 2019. Enhanced bottom-ice algal biomass across a tidal strait in the Kitikmeot Sea of the Canadian Arctic. Elementa: Science of the Anthropocene 7: 22.
https://doi.org/10.1525/elementa.361

Egbert, G.D., and Erofeeva, S.Y. 2002. Efficient inverse modeling of barotropic ocean tides. Journal of Atmospheric and Oceanic Technology 19(2):183–204.
https://doi.org/10.1175/1520-0426(2002)019%3C0183:EIMOBO%3E2.0.CO;2

Egbert, G.D., and Ray, R.D. 2000. Significant dissipation of tidal energy in the deep ocean inferred from satellite altimeter data. Nature 405(6788):775–778.
https://doi.org/10.1038/35015531

Egbert, G.D., Bennett, A.F., and Foreman, M.G. 1994. TOPEX/POSEIDON tides estimated using a global inverse model. Journal of Geophysical Research 99(C12):24821–24852.
https://doi.org/10.1029/94JC01894

Ezer, T., and Mellor, G.L. 2004. A generalized coordinate ocean model and a comparison of the bottom boundary layer dynamics in terrain-following and in z-level grids. Ocean Modelling 6(3–4):379–403.
https://doi.org/10.1016/S1463-5003(03)00026-X

Garrett, C., and Kunze, E. 2007. Internal tide generation in the deep ocean. Annual Review of Fluid Mechanics 39:57–78.
https://doi.org/10.1146/annurev.fluid.39.050905.110227

Guo, L., Wu, Y., Hannah, C.G., Petrie, B., Greenberg, D., and Niu, H. 2020. A modelling study of the ice-free tidal dynamics in the Canadian Arctic Archipelago. Estuarine, Coastal and Shelf Science 236: 106617.
https://doi.org/10.1016/j.ecss.2020.106617

Haney, R.L. 1991. On the pressure gradient force over steep topography in sigma coordinate ocean models. Journal of Physical Oceanography 21(4):610–619.
https://doi.org/10.1175/1520-0485(1991)021<0610:OTPGFO>2.0.CO;2

Hannah, C.G., Dupont, F., and Dunphy, M. 2009. Polynyas and tidal currents in the Canadian Arctic Archipelago. Arctic 62(1):83 – 95.
https://doi.org/10.14430/arctic115

Howell, S.E.L., Wohlleben, T., Dabboor, M., Derksen, C., Komarov, A., and Pizzolato, L. 2013. Recent changes in the exchange of sea ice between the Arctic Ocean and the Canadian Arctic Archipelago. Journal of Geophysical Research: Oceans 118(7):3595 – 3607.
https://doi.org/10.1002/jgrc.20265

Hughes, K.G., and Klymak, J.M. 2019. Tidal conversion and dissipation at steep topography in a channel poleward of the critical latitude. Journal of Physical Oceanography 49(5):1269 – 1291.
https://doi.org/10.1175/JPO-D-18-0132.1

Kang, D., and Fringer, O. 2012. Energetics of barotropic and baroclinic tides in the Monterey Bay area. Journal of Physical Oceanography 42(2):272 – 290.
https://doi.org/10.1175/JPO-D-11-039.1

Kundu, P.K., Cohen, I.M., and Dowling, D.R. 2012. Fluid mechanics, 5th ed. New York: Academic Press.

Le Souëf, K.E., and Allen, S.E. 2014. Physical modeling of tidal resonance in a submarine canyon. Journal of Geophysical Research: Oceans 119(2):1324 – 1343.
https://doi.org/10.1002/2013JC009612

McDougall, T.T., and Barker, P.M. 2011. Getting started with TEOS-10 and the Gibbs Seawater (GSW) Oceanographic Toolbox. SCOR/IAPSO WG127.
https://www.teos-10.org/pubs/Getting_Started.pdf

McLaughlin, F.A., Carmack, E.C., Ingram, R.G., Williams, W.J., and Michel, C. 2004. Oceanography of the Northwest Passage. In: Robinson, A.R., and Brink, K.H., eds. The sea. Cambridge, Massachusetts: Harvard University Press Vol. 14. 1211 – 1242.

Mellor, G.L., Hakkinen, S., Ezer, T., and Patchen, R. 2002. A generalization of a sigma coordinate ocean model and an intercomparison of model vertical grids. In: Pinardi, N., and Woods, J.D., eds. Ocean forecasting: Conceptual basis and applications. New York: Springer. 55 – 72.

Pawlowicz, R., Beardsley, B., and Lentz, S. 2002. Classical tidal harmonic analysis including error estimates in MATLAB using T_TIDE. Computers and Geosciences 28(8):929 – 937.
https://doi.org/10.1016/S0098-3004(02)00013-4

Pétrélis, F., Llewellyn Smith, S., and Young, W.R. 2006. Tidal conversion at a submarine ridge. Journal of Physical Oceanography 36(6):1053 – 1071.
https://doi.org/10.1175/JPO2879.1

Pringle, W.J., Wirasaet, D., Suhardjo, A., Meixner, J., Westerink, J.J., Kennedy, A.B., and Nong, S. 2018. Finite-element barotropic model for the Indian and Western Pacific Oceans: Tidal model-data comparisons and sensitivities. Ocean Modelling 129:13 – 38.
https://doi.org/10.1016/j.ocemod.2018.07.003

Prinsenberg, S.J., and Bennett, E.B. 1989. Transport between Peel Sound and Barrow Strait in the Canadian Arctic. Continental Shelf Research 9(5):427 – 444.
https://doi.org/10.1016/0278-4343(89)90008-3

Rotermund, L.M., Williams, W.J., Klymak, J.M., Wu, Y., Scharin, R.K., and Haas, C. 2021. The effect of sea ice on tidal propagation in the Kitikmeot Sea, Canadian Arctic Archipelago. Journal of Geophysical Research: Oceans 126(5): e2020JC016786.
https://doi.org/10.1029/2020JC016786

Song, Y.T. 1998. A general pressure gradient formulation for ocean models. Part I: Scheme design and diagnostic analysis. Monthly Weather Review 126(12):3213 – 3230.
https://doi.org/10.1016/0278-4343(89)90008-3

Trefethen, L.N. 2000. Spectral methods in MATLAB. Philadelphia: Society for Industrial and Applied Mathematics.

Vlasenko, V., Stashchuk, N., and Hutter, K. 2005. Baroclinic tides: Theoretical modeling and observational evidence. Cambridge: Cambridge University Press.

Williams, W., Brown, K., Bluhm, B., Carmack, E., Dalman, L., Danielson, S., Else, B., et al. 2018. Stratification in the Canadian Arctic Archipelago's Kitikmeot Sea: Biological and geochemical consequences. Polar Knowledge: Aqhaliat Report. 46 – 52.

Xu, C., Mikhael, W., Myers, P.G., Else, B., Sims, R.P., and Zhou, Q. 2021. Effects of seasonal ice coverage on the physical oceanographic conditions of the Kitikmeot Sea in the Canadian Arctic Archipelago. Atmosphere – Ocean 59(4 – 5):214 – 232.
https://doi.org/10.1080/07055900.2021.1965531